

Check for updates

Worse Interference of Fe³⁺ than Fe²⁺ on Degrading the Interphase and Performance of LiFePO₄||Graphite Battery

Jiayi Zhang, Suting Weng, Cong Zhong, Jiacheng Zhu, Yan Liu, Qiu Fang, Hao Zhang, Yejing Li,* and Xuefeng Wang*

The detrimental effects of Fe-ion crosstalk on LiFePO₄||Graphite battery performance, coupled with limited mechanistic insights into solid electrolyte interphase (SEI) evolution under such interference, warrant systematic investigation. Herein, advanced characterization techniques—including X-ray photoelectron spectroscopy, time-of-flight secondary ion mass spectrometry, and cryogenic transmission electron microscopy—are employed to reveal SEI evolution on graphite anodes under Fe²⁺/Fe³⁺ influence. Results demonstrate that Fe³⁺ exerts more severe adverse effects than Fe²⁺. Specifically, Fe²⁺ primarily promotes conventional electrolyte reduction reactions, increasing H₂, CH₄, and CO₂ generation. In contrast, Fe³⁺ facilitates radical combinations and catalyzes two-electron reductions, triggering side reactions releasing CO, C₂H₄, and C₂H₆. The SEI thickness under Fe-ion interference (Fe²⁺: 7.20-13.76 nm, Fe³⁺: 9.12-17.55 nm) significantly exceeds that of the base electrolyte (3.15-7.64 nm), with Fe deposits accumulating in organometallic forms. Critically, the presence of Fe³⁺ and its adverse impacts on battery safety and cycling stability are validated in practical pouch cells. This study uncovers the chemical nature of the dissolved Fe ion and its deposits, provides mechanistic insights into its interference with SEI properties and Li-ion battery performances, which in turn helps to mitigate such detrimental effects.

1. Introduction

LiFePO₄ (LFP) cathodes are recognized as one of the most promising cathode materials due to their low cost, inherent safety, and high reversible capacity.^[1] However, with the widespread adoption of electric vehicles and smart grids, commercial LFP||Graphite (Gr) batteries struggle to meet the increasingly stringent demands for cycle life, safety, and

other performance metrics in practical applications. [2] Fe-ion crosstalk, which significantly degrades the battery performance, has emerged as a critical issue urgently needing resolution in LFP systems. [3] Additionally, a comparative study of transition metals (TMs) revealed that Fe ions exhibit a stronger deposition propensity on Gr anodes than Mn, Ni, and Co ions, [3] further emphasizing the research value of Fe-ion crosstalk. However, compared to extensive characterizations and investigations of other TM ions (e.g., Mn²⁺) crosstalk, [4] research into Fe ions remains underexplored.

Previous investigations reveal that HF-etching LFP triggers Fe ion dissolution,^[5] which is significantly influenced by the type of lithium salts.^[4c] Jin et al. demonstrated that the Fe impurity in commercial LFP cathodes can lead to Fe dendrite formation on anodes, which contributes to internal short-circuits—a hypothesis supported by Fe-enriched points observed on the separator.^[6] Eldesoky et al. linked localized Fe accumulation to lithium

dendrite distribution via scanning micro X-ray fluorescence (μ XRF), suggesting that Fe 0 can act as an electronic conductor promoting uneven Li deposition and electrolyte decomposition. Notably, these studies failed to directly evidence the metallic Fe deposits on the anode. Tang et al. identified Fe 0 deposition on Gr anodes after 1000 cycles in pouch cells with 200 ppm Fe $^{2+}$ additions by X-ray photoelectron spectroscopy (XPS). Quantitative analysis further revealed that dissolved

J. Zhang, S. Weng, C. Zhong, J. Zhu, Y. Liu, Q. Fang, X. Wang Beijing National Laboratory for Condensed Matter Physics Institute of Physics Chinese Academy of Sciences Beijing 100190, China E-mail: wxf@iphy.ac.cn J. Zhang, J. Zhu, Q. Fang, X. Wang College of Materials Science and Opto-Electronic Technology University of Chinese Academy of Sciences Beijing 100049, China

The ORCID identification number(s) for the author(s) of this article can be found under https://doi.org/10.1002/adma.202513736

DOI: 10.1002/adma.202513736

S. Weng, X. Wang School of Physical Sciences University of Chinese Academy of Sciences Beijing 100049, China

C. Zhong, Y. Li State Key Laboratory of Advanced Metallurgy School of Metallurgical and Ecological Engineering University of Science and Technology Beijing Beijing 100083, China

E-mail: liyejing@ustb.edu.cn

Y. Liu, H. Zhang Chemical Defense Institute Beijing 100191, China

1521495. 0. Downloaded from https://advanced.onlinelibrary.wiley.com/doi/1.01002/adma.202313736 by Institute Of Physics Chinese Academy Of Sciences, Wiley Online Library on [01.09/2025]. See the Terms and Conditions (https://onlinelibrary.wiley.com/emi

Fe predominantly increases lithium alkyl carbonate content in solid electrolyte interphase (SEI), which is closely associated with the ethylene carbonate (EC) decomposition, accelerating consumption of active lithium and capacity degradation in the batteries.^[5b] However, this study did not clarify specific electrolyte decomposition pathways. Different from the conventional viewpoint, Kim et al. proposed that Fe ions migrate to silicon anodes and form stable fluorinated SEI layers (e.g., FeF₂/FeF₃ and LiF), which suppress electrolyte decomposition, thereby improving initial Coulombic efficiency (CE) and cycle life.[8] Furthermore, previous studies have seldom investigated the oxidation states of Fe ions dissolved in the electrolyte and thus know little about the potentially differential harm caused by Fe²⁺ and Fe³⁺. Therefore, for Fe-ion crosstalk, several key questions necessitate systematic investigations: 1) the chemical state of Fe ions (Fe²⁺ or Fe³⁺) in the electrolyte, 2) the precise form of Fe deposits, 3) the specific composition and structure of the SEI under Fe-ion interference, and 4) the mechanism of Fe-ion-driven electrolyte decomposition and its effects on modifying decomposition pathways. Additionally, the potential discrepancies between exogenously introduced Fe salts and practical conditions need to be clarified.

Herein, we decoupled the detrimental effects of Fe²⁺ and Fe³⁺ on battery performance by introducing these species independently into the electrolyte, revealing that Fe3+ has significantly more severe impacts than Fe²⁺. The change of Gr SEI was probed by various techniques, including XPS, cryogenic transmission electron microscopy (cryo-TEM), electron energy loss spectroscopy (EELS), and time-of-flight secondary ion mass spectrometry (ToF-SIMS). Results demonstrate that Fe ions primarily deposit as organic species on Gr surfaces and induce excessive SEI overgrowth. Through a comparison of electrochemical and chemical reactions and semi-quantitative analysis of reactiongenerated gases using gas chromatography (GC), the changes in the electrolyte decomposition pathways were investigated: Fe²⁺ amplifies regular reduction reactions while Fe3+ further facilitates radical coupling and catalyzes two-electron reduction processes. This Fe-ion-driven process markedly increases gas evolution, thus significantly compromising battery safety. Further validation via UV-vis spectroscopy and long-term cycling experiments on LFP||Gr pouch cells confirmed the presence of Fe³⁺ that degrades battery cyclability. This work provides critical insights for systematically disentangling TM-induced SEI transformation mechanisms, offering a reference for mitigating crosstalkassociated performance degradation in Li-ion batteries.

2. Results and Discussion

2.1. Electrochemical Performance with Fe2+ and/or Fe3+

To systematically evaluate the effects of different valence states of Fe ions in the electrolyte on battery performance, controlled concentrations of Fe(SO $_3$ CF $_3$) $_2$ (Fe $^{2+}$ source) or Fe(SO $_3$ CF $_3$) $_3$ (Fe $^{3+}$ source) were introduced into the base electrolyte (1 $\,\mathrm{M}$ LiPF $_6$ in 1:9 $\,\mathrm{wt}.\%$ FEC/DMC). Five modified electrolyte systems were investigated: base electrolyte (referred to as "base"), base+1000 ppm Fe $^{2+}$ ("base+Fe $^{2+}$ "), base+1000 ppm Fe $^{3+}$ ("base+Fe $^{2+}$ "), base+500 ppm Fe $^{2+}$ +500 ppm Fe $^{3+}$ ("base+Fe $^{2+}$ +Fe $^{3+}$ ") and base+0.3372 $\,\mathrm{M}$ LiSO $_3$ CF $_3$ ("base+ LiSO $_3$ CF $_3$ ") (where the

concentration of SO₃CF₃⁻ is the same as that in base+Fe³⁺). The initial voltage curves and long-term cycling performance of base+LiSO₂CF₂ are similar to those of the base electrolyte. indicating the negligible influence of the introduced SO₃CF₃⁻. The first-cycle charge-discharge profiles of LFP||Gr full cells (Figure 1a) reveal that Fe-ion additives induce a distinct lowvoltage charge plateau (<2.5 V), directly reducing the initial coulombic efficiency (CE). This effect is particularly pronounced in Fe3+-containing electrolytes. The platform corresponds to both Fe3+ reduction to the lower valence state and enhanced electrolyte decomposition on the Gr surface at lower reduction voltage. The latter leads to the excessive SEI layer formation and higher interfacial impedance, which decreases discharge capacity and further reduces CE. Consequently, the base +Fe³⁺ cell exhibits a CE of 71.57%, significantly lower than base (86.96%) and base+Fe²⁺ (84.53%). The intermediate performance of base+ $Fe^{2+}+Fe^{3+}$ (CE = 77.83%) demonstrates synergistic effects between Fe species.

Fe ions also exert significant impacts on the long-cycle performance degradation (Figure 1b,c; Table S1, Supporting Information). After 300 cycles, the base+Fe³+ cell retains only 44.08% capacity (51.38 mAh g $^{-1}$), far below base (89.54%, 124.67 mAh g $^{-1}$) and base+Fe²+ (62.50%, 85.18 mAh g $^{-1}$). The base+Fe²++Fe³+ cell exhibits intermediate capacity retention (52.94%, 66.53 mAh g $^{-1}$). The voltage profiles of the 200th and 300th cycles (Figure 1c) reveal that the addition of Fe ions, particularly Fe³+, significantly increases the polarization of the cell (from 0.14 V of the base cell to 0.19 V of the base +Fe³+ cell at the 200th cycle). This suggests to from excessive SEI formation is triggered by Fe ions, leading to continuous capacity fading.

Electrochemical impedance spectroscopy (EIS) coupled with distributed relaxation time (DRT) analysis^[9] (Figure 1d; Figure S1, Supporting Information) shows sequential increases in SEI resistance ($R_{\rm SEI}$) and charge transfer resistance ($R_{\rm ct}$) for base < base+Fe²⁺ < base+Fe³⁺, consistent with the observed capacity fading trend. Post-formation Gr anodes analyzed via inductively coupled plasma-optical emission spectrometer (ICP-OES) (Figure 1e) confirm higher Fe deposition in Fe³⁺-containing electrolyte (1199.08 ppm in base+Fe³⁺ vs 593.75 ppm in base+Fe²⁺), indicating enhanced SEI formation by Fe³⁺.

These results demonstrate that Fe^{3+} exerts more detrimental effects on both initial CE and long-term cycle performance compared to Fe^{2+} , due to stronger reductive decomposition of electrolyte promoting excessive SEI formation. The Fe^{2+}/Fe^{3+} -mixed cell exhibits intermediate performance consistent with the combined effects of both Fe species.

2.2. Interphase Chemistry and Structure with Fe²⁺ or Fe³⁺

Surface chemistry of the SEIs formed on Gr anodes after formation was investigated via XPS. Elemental composition profiles (Table S2, Supporting Information) reveal notable distinctions among electrolyte systems. In the base+Fe³+ cell, F content in the SEI increases from 39.17% (base electrolyte) to 51.14%, suggesting intensified decomposition of FEC or LiPF₆. The C 1s spectra (Figure 2a,c) can be decoupled into six peaks ascribed to C–F (\approx 290.7 eV), ROCO₂Li (\approx 289.7 eV), C=O (\approx 288.6 eV), C–O (\approx 286.6 eV), C–C (\approx 284.8 eV), and C–Li (\approx 281.9 eV). [10]

152 14095, 0, Downloaded from https://advanced.onlinelibrary.wiley.com/doi/10.1002/adma.202513736 by Institute Of Physics Chinese

Academy Of Sciences, Wiley Online Library on [01/09/2025]. See the Terms

on Wiley Online Library for rules of use; OA articles are governed by the applicable Creative Commons License

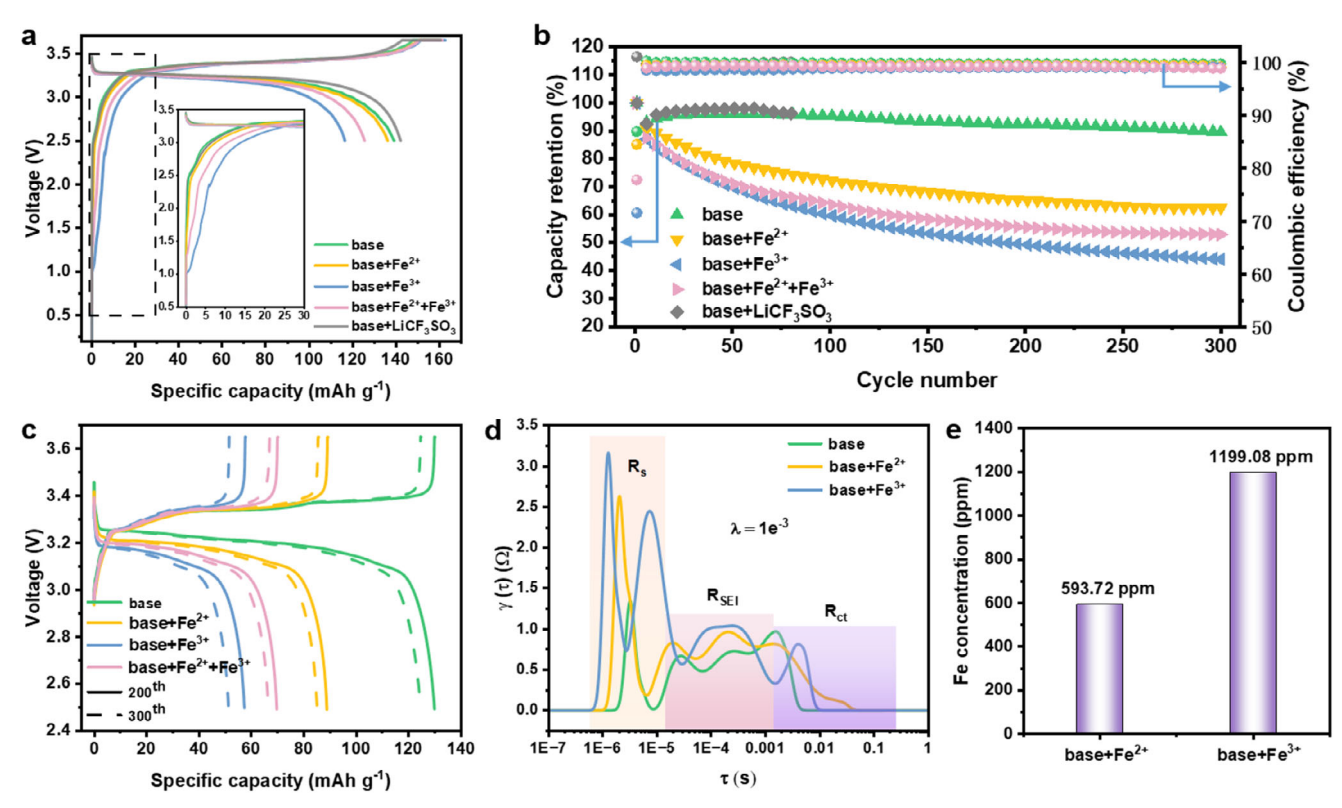


Figure 1. a) The first charge/discharge curves of the LFP||Gr full cells with base electrolyte and Fe-containing electrolytes. b) Cycle performance of the LFP||Gr full cells. c) Voltage profiles at the 200th and 300th cycles. d) The DRT results for cells with different electrolytes after formation. e) ICP-OES results of Fe concentration on the Gr anodes after formation.

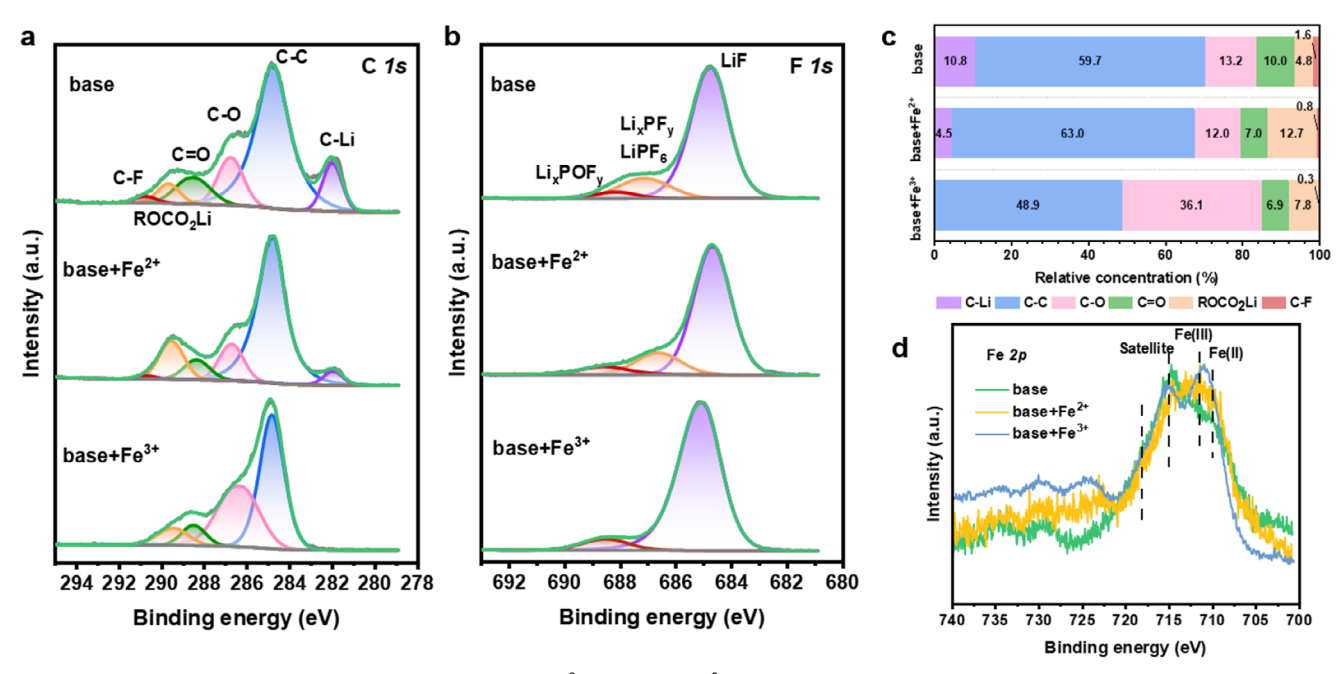


Figure 2. a, b) XPS spectra of C 1s and F 1s from base, base+ Fe^{2+} , and base+ Fe^{3+} .c) The relative atomic ratio of C—Li, C—C, C—O, C=O, ROCO₂Li, and C—F based on C 1s spectra.d) XPS spectra of Fe 2p.

15214959, O. Downloaded from https://advanced.onlinelbrary.wiley.com/doi/10.1002/sdma.202513736 by Institute Of Physics Chinese Academy Of Sciences, Wiley Online Library on [01.09.2025]. See the Terms and Condition (https://onlinelbrary.wiley.com/coi/10.1002/sdma.202513736 by Institute Of Physics Chinese Academy Of Sciences, Wiley Online Library on [01.09.2025]. See the Terms and Condition (https://onlinelbrary.wiley.com/coi/10.1002/sdma.202513736 by Institute Of Physics Chinese Academy Of Sciences, Wiley Online Library on [01.09.2025]. See the Terms and Condition (https://onlinelbrary.wiley.com/coi/10.1002/sdma.202513736 by Institute Of Physics Chinese Academy Of Sciences, Wiley Online Library on [01.09.2025]. See the Terms and Condition (https://onlinelbrary.wiley.com/coi/10.1002/sdma.202513736 by Institute Of Physics Chinese Academy Of Sciences, Wiley Online Library on [01.09.2025]. See the Terms and Condition (https://onlinelbrary.wiley.com/coi/10.1002/sdma.202513736 by Institute Of Physics Chinese Academy Of Sciences, Wiley Online Library on [01.09.2025]. See the Terms and Condition (https://onlinelbrary.wiley.com/coi/10.1002/sdma.202513736 by Institute Of Physics Chinese Academy Of Sciences, Wiley Online Library on [01.09.2025]. See the Terms and Condition (https://onlinelbrary.wiley.com/coi/10.1002/sdma.202513736 by Institute Of Physics Chinese Academy Of Sciences, Wiley Online Library on [01.09.2025]. See the Terms and Condition (https://onlinelbrary.wiley.com/coi/10.1002/sdma.202513736 by Institute Of Physics Chinese Academy Of Sciences, Wiley Online Library on [01.09.2025]. See the Terms and Condition (https://onlinelbrary.wiley.com/coi/10.1002/sdma.202513736 by Institute Of Physics Chinese Academy Of Sciences, Wiley Online Library on [01.09.2025]. See the Terms and Condition (https://onlinelbrary.wiley.com/coi/10.1002/sdma.202513736 by Institute Of Physics Chinese Academy Of Physics Chinese Aca

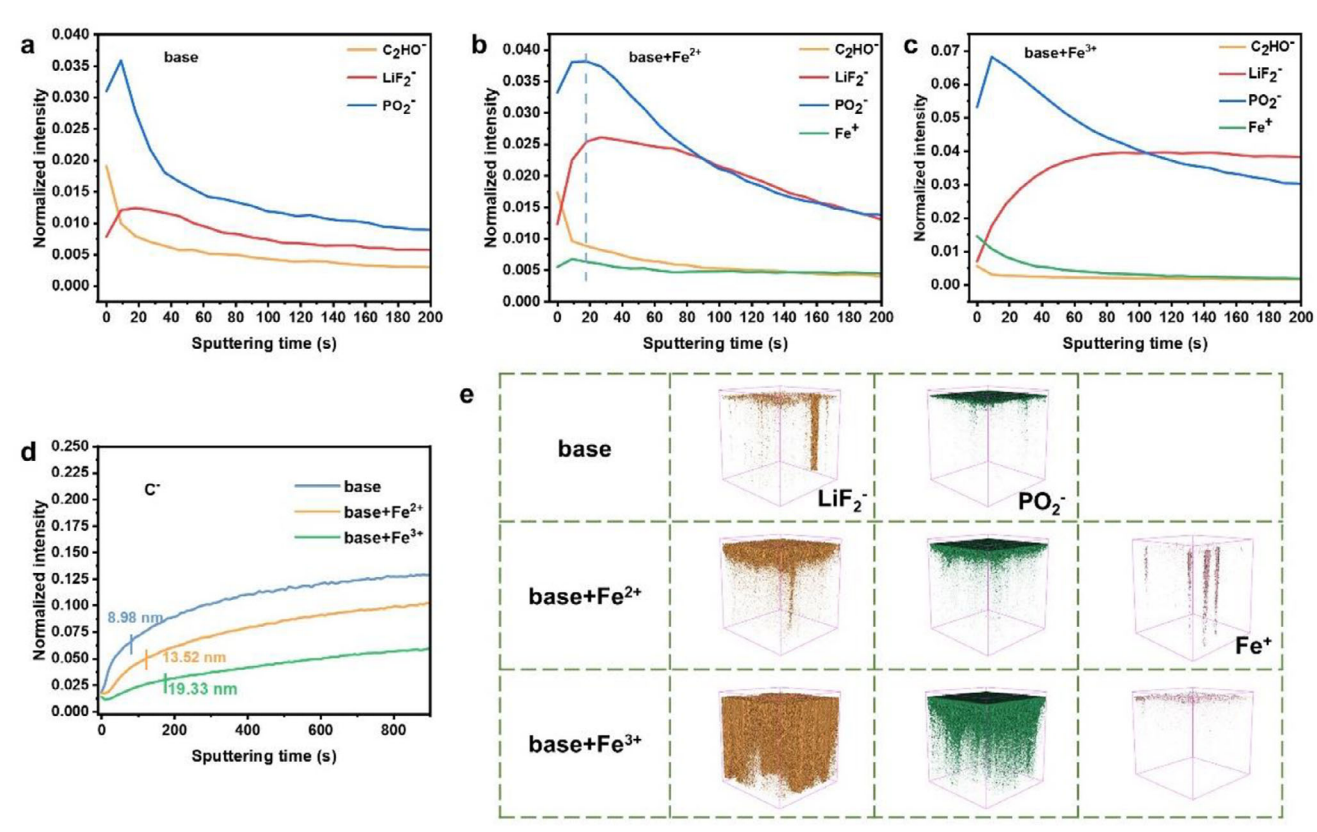


Figure 3. Normalized ToF-SIMS depth profiles of selected ion fragments sputtered from Gr anodes in a) base electrolyte, b) base+ Fe^{2+} , and c) base+ Fe^{3+} electrolytes.d) Normalized C⁻ ion depth profile and corresponding quantified SEI thickness.e) 3D compositional mapping of some sputtered ion fragments from Gr electrodes in the three electrolytes.

Compared to the base electrolyte (10.8% C-Li contribution), the C-Li signal drastically diminishes to 4.5% in base+Fe2+ and vanishes in base+Fe3+, reflective of progressively thicker SEI layers. Notably, the ROCO₂Li signal intensifies significantly in base+Fe²⁺ (12.7% vs 4.8% in the base electrolyte), while the C-O bonding peak prominently increases in base+Fe³⁺ (36.1% vs 13.2% in base). This demonstrates distinct effects of Fe2+ and Fe3+ in altering electrolyte decomposition pathways. In F 1s spectra (Figure 2b), LiF (≈684.8 eV) originates from decomposition of FEC and LiPF₆, while Li_vPOF_v (≈688.1 eV) and Li_vPF_v (≈687.2 eV) emanate from LiPF₆ reduction.^[11] With the addition of Fe ions and increasing Fe ion valence states, the relative content of Li_vPF_v decreases progressively while Li_vPOF_v increases, highlighting Fe-ion-induced alterations in LiPF₆ decomposition pathways. Additionally, LixPOF, is commonly considered a component that reduces the stability of the SEI.^[3] Lastly, Fe 2p spectra (Figure 2d) show the presence of Fe²⁺-containing compounds rather than the metallic Fe (Fe⁰) in all electrolytes.

To further investigate the composition and spatial distribution of Fe depositions within SEI layers, ToF-SIMS analyses were performed on post-formation SEI layers (**Figure 3**; Figure S2, Supporting Information). Ionic fragment depth profiles (e.g., inorganic LiF $_2$ ⁻ and organic C $_2$ HO $^-$ ions) reveal layered SEI structures (Figure 3a–c): an organic-rich outer layer and an inorganic-rich inner layer. The Fe $^+$ fragment is found preferentially localized in the outer organic layer, indicating that Fe exists within the

SEI in an organically bound configuration. SEI thickness quantification (Figure 3d) confirms progressive growth under Fe ion influence: base+Fe³⁺ yields the thickest SEI (19.33 nm), exceeding both base+Fe²⁺ (13.52 nm) and the base electrolyte (8.98 nm).

3D compositional renderings (Figure 3e; Figure S2, Supporting Information) corroborate that both inorganic (e.g., LiF $_2$ -, PO $_2$ -/PO $_3$ -) and organic components (e.g., C $_2$ HO-) are enriched in Fe-containing (particularly Fe 3 +) electrolytes, consistent with accelerated electrolyte decomposition. Additionally, PF $_6$ - content progressively decreases while PO $_2$ F $_2$ - increases across the sequence: base, base+Fe 2 +, base+Fe 3 + (Figure S2, Supporting Information). This aligns with F 1s XPS spectra (Figure 2b), confirming Fe-driven shifts in LiPF $_6$ reduction pathways toward Li $_x$ POF $_y$.

Cryo-TEM was employed to characterize the nanoscale structure of SEI layers and Fe deposits in the three electrolytes. All SEIs exhibit the characteristic feature of crystalline inorganic nanograins embedded within an amorphous matrix, and the majority of inorganic constituents are concentrated at the inner layer of SEIs, while Fe-containing electrolytes have significantly thicker SEI layers. Specifically, SEI thicknesses in base+Fe³⁺ (9.12–17.55 nm) exceed those in base electrolyte (3.15–7.64 nm) and base+Fe²⁺ (7.20–13.76 nm) (**Figure 4a–c**; Figure S3, Supporting Information), consistent with prior XPS and ToF-SIMS results. Notably, Fe distribution within SEI layers is non-uniform. Energy-dispersive X-ray spectroscopy (EDS) was first used to

15214095, 0, Downloaded from https://advanced.onlinelibrary.wiley.com/doi/10.1002/adma.202513736 by Institute Of Physics Chinese Academy Of Sciences, Wiley Online Library on [01.09/2025]. See the Terms and Conditions (https://onlinelibrary.wiley

.com/terms-and-conditions) on Wiley Online Library for rules of use; OA articles are governed by the applicable Creative Commons License

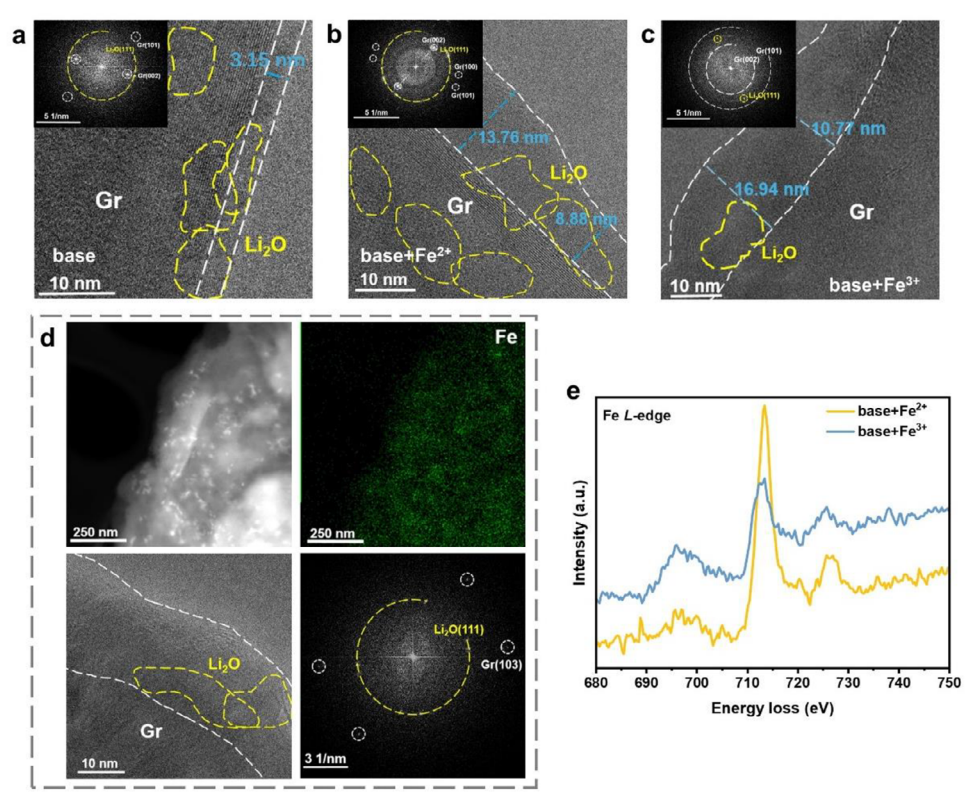


Figure 4. Cryo-TEM images of SEI layers in a) base electrolyte, b) base+Fe²⁺, and c) base+Fe³⁺ electrolytes, with corresponding FFT patterns in the inset.d) EDS elemental mapping of Fe-enriched region in SEI layer from base+Fe³⁺ electrolyte, alongside high-resolution TEM image and FFT pattern. e) EELS spectra of the Fe L-edge on Gr anodes in Fe-containing electrolytes.

identify Fe-enriched regions (e.g., Figure S4b, Supporting Information for base+Fe2+ and Figure S4c, Supporting Information for base+Fe³⁺), followed by high-resolution TEM imaging of these areas (Figure 4d; Figure S5, Supporting Information). Fast-Fourier transform (FFT) of high-resolution images from Fe-enriched zones shows none of the diffraction signatures belonging to the crystalline Fe-containing phases, apart from Gr and Li₂O, suggesting that Fe primarily exists as amorphous organometallic complexes. Furthermore, EDS analyses (Figure S4 and Table S3, Supporting Information) reveal that Fe-rich regions are accompanied by enrichment of O, F, P, and S elements, further supporting Fe's role in accelerating electrolyte decomposition. Besides the peaks at ≈535.3 eV (refer to Li₂O) and ≈536.7 eV (refer to Li₂CO₃), EELS O K-edge spectra from Fe-enriched zones in base+Fe²⁺ and base+Fe³⁺ display a distinct peak at 540.5 eV associated with the formation of Fe-O compounds (Figure S6, Supporting Information).^[13] Furthermore, the positions of Fe L_2/L_3 -edge peaks (Figure 4e) are identical regardless of the initial Fe valence (Fe²⁺/Fe³⁺) introduced into the electrolyte, which suggests that deposited Fe stabilizes at +2.^[14]

Moreover, differential scanning calorimetry (DSC) was carried out to assess the thermal stability of the SEIs.^[15] As shown in Figure S7 (Supporting Information), the SEI thermal stability decreases sequentially in the base, base+Fe²⁺, and base+Fe³⁺, thereby revealing the detrimental effect of Fe ions on battery safety.

2.3. Fe Ions Altered Electrolyte Decomposition Pathways

The compositional and structural evolution of SEI in Fecontaining electrolytes is inherently intertwined with the reduction pathways of the electrolytes. The Fe ions are inclined to coordinate with FEC or DMC, causing the red shift observed via Raman spectroscopy (Figure S8, Supporting Information), which acts as a precursor to enhance electrolyte reduction activity. Furthermore, linear sweep voltammetry (LSV) was performed across the three electrolytes (Figure \$9a, Supporting Information), while pure solvents (FEC, DMC) and their Fe-containing counterparts were also tested (Figure S9b,c, Supporting Information) to decouple cooperative solvent effects. These analyses attribute four distinct reduction peaks to FEC species with varying coordination states, proving the coordination between Fe ions and FEC. Specifically, when FEC coordinates with Fe³⁺, its reduction voltage shifts from $\approx 1.2 \text{ V}$ (vs Li/Li⁺)[16] to $\approx 2.5 \text{ V}$ (vs Li/Li⁺). Notably, the presence of Fe³⁺ simultaneously catalyzes FEC decomposition across all coordination conditions, significantly amplifying the corresponding reduction peaks.

To investigate the decomposition mechanisms of electrolyte components, Fe-containing electrolytes were chemically reacted with the fully lithiated Gr (LiC₆) electrodes (**Figure 5a**). To bridge chemical and electrochemical processes, XPS analysis was performed on reacted samples (Figure 5b; Figure S10 and Table S4, Supporting Information) and cross-referenced with

1521495, 0, Downloaded from https://advanced.onlinelibrary.wikey.com/obi/10.1092/adma.202513736 by Institute Of Physics Chinese Academy Of Sciences, Wiley Online Library on [01.09/2025]. See the Terms and Conditions (https://onlinelibrary.wikey.com/ebi/10.1092/adma.202513736 by Institute Of Physics Chinese Academy Of Sciences, Wiley Online Library on [01.09/2025]. See the Terms and Conditions (https://onlinelibrary.wikey.com/ebi/10.1092/adma.202513736 by Institute Of Physics Chinese Academy Of Sciences, Wiley Online Library on [01.09/2025]. See the Terms and Conditions (https://onlinelibrary.wikey.com/ebi/10.1092/adma.202513736 by Institute Of Physics Chinese Academy Of Sciences, Wiley Online Library on [01.09/2025]. See the Terms and Conditions (https://onlinelibrary.wikey.com/ebi/10.1092/adma.202513736 by Institute Of Physics Chinese Academy Of Sciences, Wiley Online Library on [01.09/2025]. See the Terms and Conditions (https://onlinelibrary.wikey.com/ebi/10.1092/adma.202513736 by Institute Of Physics Chinese Academy Of Sciences, Wiley Online Library on [01.09/2025]. See the Terms and Conditions (https://onlinelibrary.wikey.com/ebi/10.1092/adma.202513736 by Institute Of Physics Chinese Academy Of Sciences, Wiley Online Library on [01.09/2025]. See the Terms and Conditions (https://onlinelibrary.wikey.com/ebi/10.1092/adma.202513736 by Institute Of Physics Chinese Academy Of Sciences, Wiley Online Library on [01.09/2025]. See the Terms and Conditions (https://onlinelibrary.wikey.com/ebi/10.1092/adma.202513736 by Institute Of Physics Chinese Academy Of Sciences, Wiley Online Library on [01.09/2025]. See the Terms and Conditions (https://onlinelibrary.wikey.com/ebi/10.1092/adma.202513736 by Institute Of Physics Chinese Academy Of Sciences, Wiley Online Library on [01.09/2025]. See the Terms and Conditions (https://onlinelibrary.wikey.com/ebi/10.1092/adma.202513736 by Institute Of Physics Chinese Academy Of Sciences, Wiley Online Library on [01.09/2025]. See the Terms and Conditions (https://onlinelibrary.wikey.c

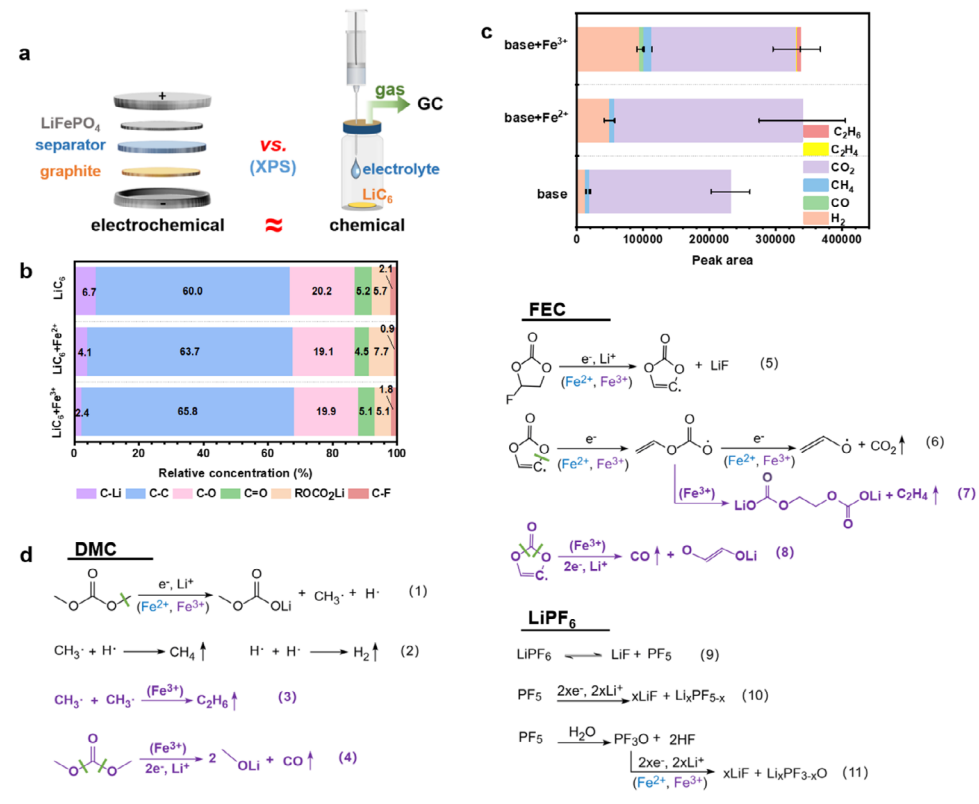


Figure 5. a) Schematic diagram showing the bridge between chemical and electrochemical reactions.b) The relative atomic ratio of C—Li, C—C, C—O, C—O, ROCO₂Li, and C—F after chemical reaction based on C 1s spectra.c) GC-derived quantitative analysis of gas species via peak area integration. d) Electrolyte component decomposition pathways with corresponding stoichiometric equations.

post-formation spectra (Figure 2), revealing strong agreement between chemical and electrochemical behaviors (Figure 5a). This demonstrates that findings from chemical reaction studies can be largely extrapolated to electrochemical systems.

Notably, the base+Fe³⁺ electrolyte demonstrates more vigorous reactions compared to base+Fe²⁺ (Figures S11 and S12, Supporting Information). Gas evolution during the chemical reaction process was quantified via GC analysis (Figure 5c; Figure S13 and Table \$5, Supporting Information). After the reaction taking place in a sealed container for 30 min, GC results reveal sequential increases in H2 and CH4 concentrations among the tested electrolytes: base (H2 peak area: 14353, CH4 peak area: 6859), base+Fe²⁺ (H₂: 41346, CH₄: 8137), and base+Fe³⁺ (H₂: 99516, CH₄: 11573). CO₂ production peaks in base+Fe²⁺ (347320), exceeding both base (182585) and base+Fe³⁺ (253780) conditions. A critical distinction is observed: CO, C2H4, and C2H6 are exclusively detected under Fe3+ conditions. This highlights that Fe²⁺ primarily enhances reaction intensity within conventional pathways in base electrolyte, which generate H₂, CH₄ and CO₂, whereas Fe³⁺ catalyzes decomposition pathways generating additional gaseous byproducts. The variations in gas production volume and product composition across different electrolytes during chemical reactions provide crucial experimental evidence for deducing the mechanisms underlying electrochemical reactions.

Based on the components of the SEI layers and GC results, the decomposition pathways of various substances in the electrolyte were proposed (Figure 5d).^[17] In the base and base+Fe²⁺

electrolytes, the initial reactions of DMC and FEC primarily involve one-electron reactions (Reactions (1) and (5)), generating radicals that subsequently combine or further decompose to produce CH₄ and H₂ (Reaction (2)) and CO₂ (Reaction (6)). The higher electronegativity of Fe³⁺ enables a stronger attraction to radicals, and its larger coordination number and binding strength increase the probability of radical combination. As shown in Reactions (3) and (7), this mechanism in the base+Fe³⁺ system leads to the formation of C_2H_6 and C_2H_4 . Additionally, Reaction (7) elevates the C-O bond content in the SEI layer, consistent with XPS results (Figure 2a). Reaction (7) partially suppresses Reaction (6), which explains the slightly lower CO₂ production in the base+Fe³⁺ system compared to base+Fe²⁺. CO originates from two-electron reactions of DMC and FEC induced by Fe3+ (Reactions (4) and (8)). Furthermore, Fe-ion-driven decomposition of LiPF₆ increases the generation of Li_xPOF_v species, as evidenced by XPS and ToF-SIMS analyses. The decomposition pathways of LiPF₆ are outlined in Reactions (9-11).[18]

Therefore, Fe ions lower the reduction voltage and enhance the reductive activity of FEC through coordination. Fe ions concurrently promote DMC decomposition and redirect LiPF₆ decomposition pathways. As for the decomposition of FEC and DMC, Fe²⁺ primarily intensifies existing electrolyte reduction reactions while Fe³⁺ facilitates radical combination and catalyzes two-electron reductions, introducing side reaction mechanisms. The elevated gaseous byproducts induced by Fe ions pose risks

ununu advimat de

15214095, 0, Downloaded from https://advanced.onlinelibrary.wiley.com/doi/10.1002/adma.202513736 by Institute Of Physics Chinese Academy Of Sciences, Wiley Online Library on [01.09.2025]. See the Terms and Conditions (https://onlinelibrary.wiley

-and-conditions) on Wiley Online Library for rules of use; OA articles are governed by the applicable Creative Commons License

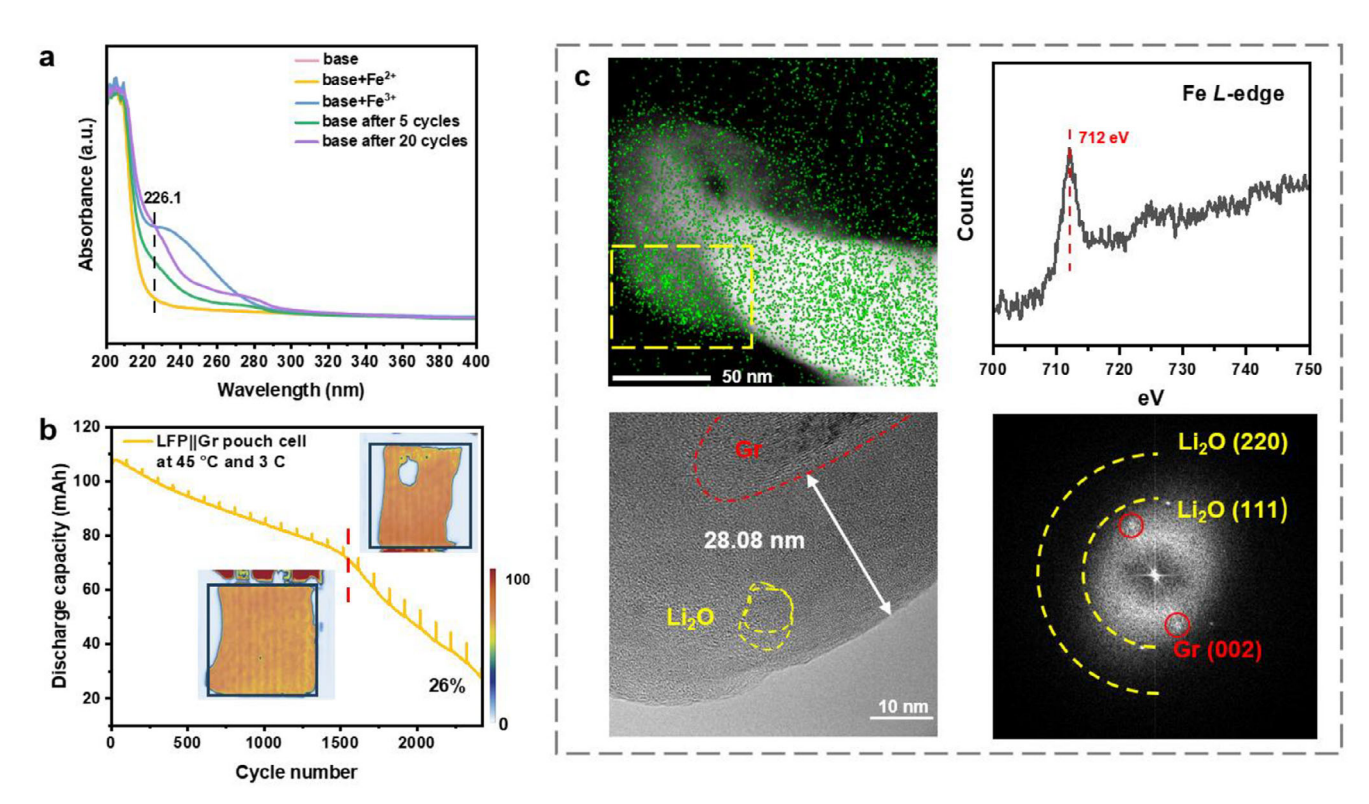


Figure 6. a) UV–vis absorbance analysis of the electrolytes extracted from coin cells cycled under base electrolyte for 5 and 20 cycles with some referenced solutions: base electrolyte, base+ Fe^{2+} , and base+ Fe^{3+} . b) Long-term cycling performance and capacity retention of LFP||Gr pouch cell and ultrasonic analyses (inset) prior to capacity plunge and immediately post-plunge. (The color bar indicates the degree of electrolyte wetting, with red representing complete wetting and white denoting the absence of electrolyte.). c) Cryo-TEM characterization (including elemental mapping of Fe distribution, Fe L-edge EELS spectra, high-resolution image, and FFT diffraction pattern) of Fe-enriched anode surface region (LFP||Gr pouch cell after 2425 cycles).

to long-term cycling stability. Additionally, chemical reactions between Fe ions and LiC_6 lead to active lithium loss, diminishing reversible capacity.

2.4. Crosstalk of Fe3+ under Practical Conditions

The distinct electrochemical behaviors of Fe²⁺ and Fe³⁺ highlighted in the above experiments necessitate confirmation of Feion's valence state in electrolyte under practical conditions. UV–vis absorbance spectra were employed to track Fe ion speciation. While no absorbance differences are observed between base and base+Fe²⁺ electrolytes, base+Fe³⁺ displays a distinct absorbance peak at 229 nm, confirming this feature as a diagnostic marker for Fe³⁺ presence (**Figure 6a**; Figure S14, Supporting Information). To investigate Fe dissolution during cycling, electrolytes in the base cells without adding Fe ions were analyzed by testing the electrolyte extracted from cells cycled for 5 and 20 cycles by UV–vis spectroscopy. Fe³⁺ absorption at 226.1 nm is detected and increased with cycling time (Figure 6a). The collective data demonstrate that it is Fe³⁺ that persists in the electrolyte during practical cycling.

While controlled electrolyte experiments provide mechanistic insights, they inherently introduce experimental settings distinct from practical operating conditions. To bridge this gap, practical LFP||Gr pouch cells (≈ 100 mAh) were used, and their capacity

retention is 26% after 2425 cycles at 45 °C and 3C (Figure 6b). Cryo-TEM observations of Fe-enriched regions on the anode surface (Figure 6c; Figure S15 and Table S6, Supporting Information) demonstrate amorphous Fe deposits within the SEI films: no crystalline lattice fringes corresponding to inorganic Fe compounds appear in high-resolution imaging, and no Fe-related diffraction spots are detected in FFT patterns. Fe L-edge spectra obtained via EELS (Figure 6c) show no peak shifting compared to samples formation in base+Fe²⁺ or base+Fe³⁺, suggesting that Fe deposits maintain a consistent valence state across different experimental conditions.

Even without intentional Fe-ion introduction, Fe-ion crosstalk significantly compromises battery cycle stability in practical use. A primary cause is that Fe ions accelerate gas byproduct accumulation within the cell, degrading electrolyte wettability. After 1500 cycles, the LFP||Gr pouch cell exhibits a sharp capacity plunge (Figure 6b), a reproducible outcome confirmed in multiple trials (Figure S16, Supporting Information). Ultrasonic imaging of pre- and post-capacity-plunge pouch cells (Figure 6b) reveals significantly increased gas bubbles and uneven electrolyte distribution post-failure. These results indicate that gas accumulation in the pouch cell reaches a critical threshold near the 1500th cycle, inducing severe electrolyte wetting deterioration. Since Fe ions catalyze gaseous byproduct generation, these findings directly highlight the detrimental impact of Fe-ion crosstalk on practical pouch cell performance.

1521495, 0, Downloaded from https://advanced.onlinelibrary.wikey.com/obi/10.1092/adma.202513736 by Institute Of Physics Chinese Academy Of Sciences, Wiley Online Library on [01.09/2025]. See the Terms and Conditions (https://onlinelibrary.wikey.com/ebi/10.1092/adma.202513736 by Institute Of Physics Chinese Academy Of Sciences, Wiley Online Library on [01.09/2025]. See the Terms and Conditions (https://onlinelibrary.wikey.com/ebi/10.1092/adma.202513736 by Institute Of Physics Chinese Academy Of Sciences, Wiley Online Library on [01.09/2025]. See the Terms and Conditions (https://onlinelibrary.wikey.com/ebi/10.1092/adma.202513736 by Institute Of Physics Chinese Academy Of Sciences, Wiley Online Library on [01.09/2025]. See the Terms and Conditions (https://onlinelibrary.wikey.com/ebi/10.1092/adma.202513736 by Institute Of Physics Chinese Academy Of Sciences, Wiley Online Library on [01.09/2025]. See the Terms and Conditions (https://onlinelibrary.wikey.com/ebi/10.1092/adma.202513736 by Institute Of Physics Chinese Academy Of Sciences, Wiley Online Library on [01.09/2025]. See the Terms and Conditions (https://onlinelibrary.wikey.com/ebi/10.1092/adma.202513736 by Institute Of Physics Chinese Academy Of Sciences, Wiley Online Library on [01.09/2025]. See the Terms and Conditions (https://onlinelibrary.wikey.com/ebi/10.1092/adma.202513736 by Institute Of Physics Chinese Academy Of Sciences, Wiley Online Library on [01.09/2025]. See the Terms and Conditions (https://onlinelibrary.wikey.com/ebi/10.1092/adma.202513736 by Institute Of Physics Chinese Academy Of Sciences, Wiley Online Library on [01.09/2025]. See the Terms and Conditions (https://onlinelibrary.wikey.com/ebi/10.1092/adma.202513736 by Institute Of Physics Chinese Academy Of Sciences, Wiley Online Library on [01.09/2025]. See the Terms and Conditions (https://onlinelibrary.wikey.com/ebi/10.1092/adma.202513736 by Institute Of Physics Chinese Academy Of Sciences, Wiley Online Library on [01.09/2025]. See the Terms and Conditions (https://onlinelibrary.wikey.c

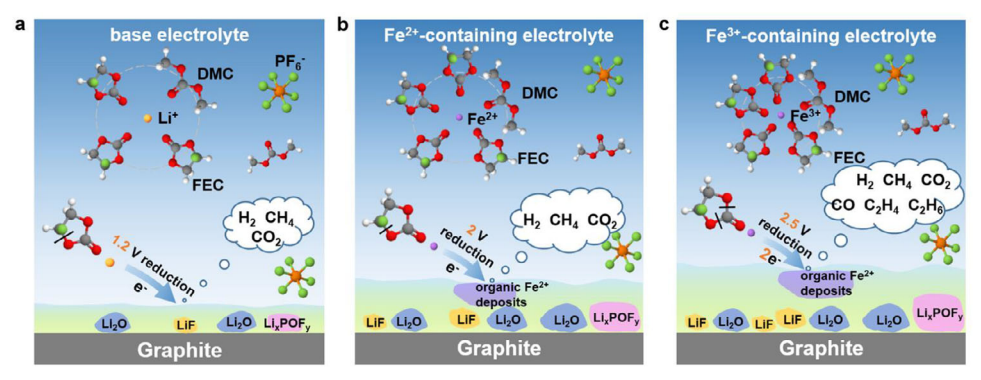


Figure 7. Schematic of the activity of Fe²⁺ and Fe³⁺ in the base electrolyte and catalytic-derived SEI structure by Fe ions.

In summary, under practical battery operating conditions, Fe ion dissolution from the cathode releases Fe³+ into the electrolyte, which has more detrimental effects on the electrochemical system than Fe²+ (Figure 7). Compared to the base electrolyte, Fe²+ accelerates electrolyte decomposition without altering the reaction pathway, leading to a thicker SEI layer. In contrast, Fe³+ facilitates radical recombination and catalyzes two-electron reduction, introducing new side reaction pathways. This results in additional gas evolution (CO, C_2H_4 , C_2H_6), the highest total gas volume, and the thickest SEI layer. Fe ions of different valence states subsequently deposit as organic complexes onto the SEI. Through this mechanism, dissolved Fe ions increase interfacial resistance, impair charge/discharge kinetics, reduce safety margins, and become a primary factor in the sudden capacity degradation observed during long-term cycling.

Fe-ion crosstalk significantly impairs battery capacity, cyclability, and safety. Therefore, developing strategies to neutralize these detrimental effects is essential. In this work, we demonstrated the feasibility of artificial SEI engineering by first preforming SEI films on Gr anodes in the base electrolyte at 0.2C, then switching the electrolyte to Fe³⁺-containing formulations. This approach increases capacity retention to 75.3% after 250 cycles in base+Fe³⁺, compared to 59.8% without the pre-formed SEI—verifying the efficacy of this intervention (Figure S17, Supporting Information).

3. Conclusion

Through a controlled introduction of Fe ions into the electrolyte, this study systematically examined the detrimental effects of Feion crosstalk on CE, interfacial impedance, and cycling stability in LFP||Gr full cells, emphasizing that Fe³⁺ induces more severe adverse impacts compared to Fe2+. In-depth analyses bridged the divide between experimental settings and practical applications. Under practical operating conditions, Fe ions dissolved from the cathode contain Fe³⁺ species, exhibiting unexpected stability in the electrolyte. Subsequently, Fe cations deposit into the SEI film in organometallic form. This process triggers excessive electrolyte decomposition and SEI overgrowth: Fe²⁺ primarily enhances existing electrolyte reduction reactions while Fe3+ facilitates radical combination and catalyzes two-electron reduction, introducing pathways for side reactions. Consequently, Fe³⁺ induces thicker SEI films and increases gaseous byproducts, advancing the onset of capacity plunge and heightening safety risks. Our work also validates the feasibility of artificial SEI engineering to mitigate Fe-ion crosstalk damage. Overall, through a systematic investigation of the TM ion crosstalk mechanism on the anode side, the research provides valuable reference for seeking tactics to mitigate the relevant harmful effects.

4. Experimental Section

Materials Preparation: Battery-grade lithium hexafluorophosphate (LiPF₆), dimethyl carbonate (DMC), and fluoroethylene carbonate (FEC) were ordered from Shangdong HiRong Power Supply Material. Co., LTD. The Gr electrode was prepared by mixing graphite powder (99.9%, Aladdin), acetylene black, and polyvinylidene fluoride (PVDF) dissolved in N-methyl pyrrolidone (NMP) at a weight ratio of 8:1:1 and then casting the slurry onto the copper foil. The prepared electrodes were dried at 55 °C for 4 h and further dried under vacuum at 120 °C for at least 6 h before use. For full coin cells, the electrode was punched with a diameter of 13 mm and an areal loading of ≈8.7 mg cm⁻². The LiFePO₄ electrode was prepared by mixing LiFePO₄ powder, acetylene black, and PVDF dissolved in NMP at a weight ratio of 8:1:1 and then casting the slurry onto the aluminum (Al)

Electrochemical Measurements: The cells were assembled in an argonpurged glovebox. For full coin cells, the electrolyte volume was maintained at 150 µL. Glass fiber filters (Whatman) and cellulose separators were employed as interlayers. The cells were rested for at least 4 h at 25 °C before cycling. Initial formation cycling involved a protocol of constant-current constant-voltage (CC-CV) charging at 0.33C followed by constant-current (CC) discharging at 0.33C for one cycle. Subsequent cycling proceeded with CC-CV charging at 0.33C and CC discharging at 1C. C-rates were calculated based on a theoretical specific capacity of LiFePO₄ (170 mAh g^{-1}). The testing was performed using the Neware Battery Testing System (CT-4008Tn-5V1A-S1-F, Shenzhen). EIS tests were carried out on the electrochemical workstation (BioLogic SP-200 system, France) with an a.c. signal of 10 mV in a frequency range from 1 MHz to 100 mHz at 25 °C. The DRT method was grounded on the premise that all impedance functions, in accordance with the Kramers-Kronig relations, can be represented as a series of infinitesimal differential RC-elements. The DRT fitting was performed with a regularization parameter $\gamma = 1 \times 10^{-3}$. LSV was performed in Gr||Li half cells, and the scanning speed is 0.1 mV s⁻¹.

Characterizations—XPS: The XPS analysis was conducted on a Thermo Fisher ESCALAB 250 Xi, using monochromatic 150 W (Al K α line) radiation. The peak positions were calibrated based on the C 1s C—C peak (284.8 eV). The sealed vessel containing the samples was transferred from the glove box to the vacuum chamber before the XPS measurements.

Characterizations—ToF-SIMS: The ToF-SIMS analysis was performed using a PHI nanoToF II Time-of-Flight Secondary Ion Mass Spectrometer. Measurements were conducted in positive/negative ion mode with a Bi³⁺ primary ion beam operated at 30 keV acceleration energy and 2 nA current. The instrument was set to high mass resolution mode (mass

15214095, 0, Downloaded from https://advanced.onlinelibrary.wiley.com/doi/10.1002/adma.202513736 by Institute Of Physics Chinese Academy Of Sciences, Wiley Online Library on [01/09/2025]. See the Terms and Conditions (https://doi.org/10.1002/adma.202513736 by Institute Of Physics Chinese Academy Of Sciences, Wiley Online Library on [01/09/2025]. See the Terms and Conditions (https://doi.org/10.1002/adma.202513736 by Institute Of Physics Chinese Academy Of Sciences, Wiley Online Library on [01/09/2025]. See the Terms and Conditions (https://doi.org/10.1002/adma.202513736 by Institute Of Physics Chinese Academy Of Sciences, Wiley Online Library on [01/09/2025]. See the Terms and Conditions (https://doi.org/10.1002/adma.202513736 by Institute Of Physics Chinese Academy Of Sciences, Wiley Online Library on [01/09/2025]. See the Terms and Conditions (https://doi.org/10.1002/adma.202513736 by Institute Of Physics Chinese Academy Of Sciences, Wiley Online Library on [01/09/2025]. See the Terms and Conditions (https://doi.org/10.1002/adma.202513736 by Institute Of Physics Chinese Academy Of Sciences, Wiley Online Library on [01/09/2025]. See the Terms and Conditions (https://doi.org/10.1002/adma.202513736 by Institute Of Physics Chinese Academy Of Sciences, Wiley Online Library on [01/09/2025]. See the Terms and Conditions (https://doi.org/10.1002/adma.20251374 by Institute Of Physics Chinese Academy Of Sciences, Wiley Online Library on [01/09/2025]. See the Terms and Conditions (https://doi.org/10.1002/adma.20251374 by Institute Of Physics Chinese Academy Of Sciences, Wiley Online Library on [01/09/2025]. See the Terms and Conditions (https://doi.org/10.1002/adma.20251374 by Institute Of Physics Chinese Academy Of Sciences, Wiley Online Library on [01/09/2025]. See the Terms and Conditions (https://doi.org/10.1002/adma.20251374 by Institute Of Physics Chinese Academy Of Sciences, Wiley Online Library on [01/09/2025]. See the Terms and Conditions (https://doi.org/10.1002/adma.20251374 by Institute Of Physics Chinese Of

-and-conditions) on Wiley Online Library for rules of use; OA articles are governed by the applicable Creative Commons License

range: 2–1850 u) with spectral data acquired over a 100 $\mu m \times$ 100 μm raster area for 5 min. For depth profiling, a 400 $\mu m \times$ 400 μm Ar⁺ sputter raster (3 kV, 100 nA) was applied for 9 s prior to analysis, followed by 1 min of ion beam deposition for depth profile acquisition. Calculation of the SEI thickness:

$$d = x \times 0.125 \tag{1}$$

$$y = (y2 - y1) \times 70\% + y1$$
 (2)

where d is the thickness of the SEI; γ_1 is the signal intensity of C⁻ before sputtering begins; γ_2 is the signal intensity of C⁻ in the Gr phase; x is the horizontal coordinate corresponding to γ .

Characterizations—Cryo-TEM: Cryo-TEM experiments were performed on a JEOL JEM-F200 operated at an accelerating voltage of 200 kV. The Gr powder samples were scraped from the electrode sheets, rinsed with DMC, and then loaded on the TEM grids. Then, the sample was placed on the cryo-TEM holder (Fischione 2550) with a tip retraction device in the glove box and then transferred into the JEOL JEM-F200 microscope without exposure to air, using a sealing sleeve. Liquid nitrogen was added to the cryo-TEM holder, and the sample temperature was dropped and maintained at ≈-180 °C. Cryo-TEM images were acquired by a Gatan Rio camera, with the electron beam dose rate being lower than 500 e $Å^{-2}$ s⁻¹ and the acquisition time was 0.25 s. The EELS spectra were acquired on a GIF Continuum 1077 in Dual EELS mode with a dispersion of 0.3 eV/channel. The EELS maps were acquired with a pixel size of 1×1 nm, a dwell time of 0.1 s, and a camera length of 200 mm. This setup allowed for the simultaneous acquisition of Li K-edge, C K-edge, and O K-edge, with the low-loss centered on the zero-loss peak and the core-loss centered on the C K-edge. To ensure accuracy, energy drift during spectrum imaging was addressed by centering the zero-loss peak to 0 eV at each pixel. Further analysis of the Gr structure and other species was carried out using Digital Micrograph (DM; Gatan) software.

Characterizations—DSC: DSC (NETZSCH STA 449 F3) measurements were carried out from 25 to 400 °C at a rate of 5 °C min⁻¹. The Gr powder was scraped from the DMC-rinsed electrode sheets, and 10 mg of the collected Gr was weighed out for DSC analysis.

Characterizations—Raman: The Raman spectra of the electrolytes were recorded on a LabRAM HR Evolution Raman spectrometer (532 nm radiation) with a resolution of 2 cm⁻¹.

Characterizations—GC Measurement: The gas evolution during the chemical reaction process was probed using a gas chromatograph (Shimadzu Nexis GC-2030) equipped with a barrier ionization discharge (BID) detector. Helium (99.9999%) was used as the carrier gas. The split temperature was kept at 250 °C and the BID detector was held at 280 °C with a gas flow of 8.07 mL min $^{-1}$. A gas-tight syringe was used to transfer the resultant gas (50 μ L) released in the chemical reaction from the container into the GC system. The test protocol lasted a total of 20 min and comprised a temperature program and a pressure program. Column temperature: 35 °C (2.5 min)–20 °C min $^{-1}$ –250 °C (0 min)–15 °C min $^{-1}$ –270 °C (5.42 min). Pressure program: 250 kPa (2.5 min)–15 kPa min $^{-1}$ –400 kPa (7.5 min) (He).

Characterizations—UV—vis: The UV—vis spectra were acquired on a Cary 60 Agilent spectrometer. The electrolytes were tested after being diluted to 1%. To investigate Fe dissolution during cycling, coin cells operated in the base electrolyte were disassembled after 5 and 20 cycles. Wash solutions from non-cathode components (anodes, separators, and casings) were tested.

Characterizations—Ultrasonic Testing: To capture the ultrasonic image, an ultrasonic battery scanner (FeLi-1200, from Beijing Wanlong Jingyi Technology Co., Ltd) was applied to accomplish the test. The FeLi-1200 main consists of an acoustic medium module, motion module, and data acquisition module. The pouch cell was fixed in the low-viscosity silicone oil bath. For the 2.5 MHz transducers, a 100 V impulse served as the driving signal. In this work, 0.2 mm precision was chosen to perform the experiment.

Supporting Information

Supporting Information is available from the Wiley Online Library or from the author.

Acknowledgements

This work was supported by the National Key Research and Development Program of China (Grant No. 2022YFB2502200), the National Natural Science Foundation of China (NSFC Nos. 52172257 and 22409211), the China Postdoctoral Science Foundation (No. 2023M743739), the Postdoctoral Fellowship Program of CPSF (No. GZC20232939), and the CAS Youth Interdisciplinary Team. The author would like to thank Gangqin Liu and Xiuqi Chen from the Institute of Physics, Chinese Academy of Sciences, for their assistance in testing the valence of deposited Fe in SEIs.

Conflict of Interest

The authors declare no conflict of interest.

Author Contributions

X.W. and J.Z. conceived the idea and designed the project. S.W. conducted partial cryo-TEM characterization. C.Z. performed XPS measurements. J.Z. conducted Raman spectroscopy. J.Z. performed all the other data collection and analysis. S.W., C.Z., Y.L., Q.F., H.Z., and Y.L. contributed to discussions and interpretation of results. X.W. and J.Z. co-wrote the manuscript, with input from all authors.

Data Availability Statement

The data that support the findings of this study are available from the corresponding author upon reasonable request.

Keywords

battery degradation, Fe²⁺/Fe³⁺ crosstalk, lithium-ion battery, SEI growth

Received: July 17, 2025 Revised: August 20, 2025 Published online:

- a) X. Chen, L. Yuan, S. Yan, X. Ma, Chem. Eng. J. 2023, 471, 144343;
 b) G. Ji, J. Wang, Z. Liang, K. Jia, J. Ma, Z. Zhuang, G. Zhou, H.-M. Cheng, Nat. Commun. 2023, 14, 584.
- [2] X. Wang, A. Yu, T. Jiang, S. Yuan, Q. Fan, Q. Xu, Adv. Mater. 2024, 36, 2410482.
- [3] S. Yoon, S.-J. Chang, K. Ahn, M. Kim, J. Mater. Chem. A 2025, 13, 13100.
- [4] a) C. Zhan, T. Wu, J. Lu, K. Amine, Energy Environ. Sci. 2018, 11, 243; b) C. Delacourt, A. Kwong, X. Liu, R. Qiao, W. L. Yang, P. Lu, S. J. Harris, V. Srinivasan, J. Electrochem. Soc. 2013, 160, A1099; c) A. Arifiadi, L. Wichmann, T. Brake, C. Lechtenfeld, J. Buchmann, F. Demelash, P. Yan, G. Brunklaus, I. Cekic-Laskovic, S. Wiemers-Meyer, M. Winter, J. Kasnatscheew, Small 2024, 21, 2410762; d) S. Komaba, N. Kumagai, Y. Kataoka, Electrochim. Acta 2002, 47, 1229; e) C. Zhan, J. Lu, A. Jeremy Kropf, T. Wu, A. N. Jansen, Y.-K. Sun, X. Qiu, K. Amine, Nat. Commun. 2013, 4, 2437; f) R. Sim, L. Su, A. Dolocan, A. Manthiram, Adv. Mater. 2024, 36, 2311573.



www.advancedsciencenews.com

ADVANCED MATERIALS

www.advmat.de

15214095, 0, Downloaded from https://advanced.onlinelibrary.wiley.com/doi/10.1002/adma.202513736 by Institute Of Physics Chinese Academy Of Sciences, Wiley Online Library on

[01/09/2025].

. See the Terms

on Wiley Online Library for rules of use; OA articles are governed by the applicable Creative Commons License

- [5] a) Y. Song, L. Wang, L. Sheng, D. Ren, H. Liang, Y. Li, A. Wang, H. Zhang, H. Xu, X. He, Energy Environ. Sci. 2023, 16, 1943; b) S. Tang, Y. Liang, Y. Peng, Y. Hu, Y. Liao, X. Yang, H. Zhang, Y. Lin, K. Zhang, J. Liang, B. Li, G. Zhao, Y. Wei, Z. Gong, Y. Yang, Adv. Energy Mater. 2025, 15, 2402842.
- [6] H.-F. Jin, Z. Liu, Y.-M. Teng, J.-k. Gao, Y. Zhao, J. Power Sources 2009, 189, 445.
- [7] A. Eldesoky, E. R. Logan, M. B. Johnson, C. R. M. McFarlane, J. R. Dahn, J. Electrochem. Soc. 2020, 167, 130539.
- [8] M. Kim, S. P. Harvey, Z. Huey, S.-D. Han, C.-S. Jiang, S.-B. Son, Z. Yang, I. Bloom, Energy Storage Mater. 2023, 55, 436.
- [9] a) Z. Zhang, J. Hu, Y. Hu, H. Wang, H. Hu, J. Colloid Interface Sci. 2024, 669, 305; b) J. Zhu, M. Knapp, X. Liu, P. Yan, H. Dai, X. Wei, H. Ehrenberg, IEEE Trans. Transp. Electrif. 2021, 7, 410.
- [10] a) V. A. Agubra, J. W. Fergus, J. Power Sources 2014, 268, 153; b) R. Dedryvère, L. Gireaud, S. Grugeon, S. Laruelle, J. M. Tarascon, D. Gonbeau, J. Phys. Chem. B 2005, 109, 15868.
- [11] a) R. Dedryvère, S. Laruelle, S. Grugeon, L. Gireaud, J. M. Tarascon, D. Gonbeau, J. Electrochem. Soc. 2005, 152, A689; b) Y. Peng, C. Zhong, M. Ding, H. Zhang, Y. Jin, Y. Hu, Y. Liao, L. Yang, S. Wang, X. Yin, J. Liang, Y. Wei, J. Chen, J. Yan, X. Wang, Z. Gong, Y. Yang, Adv. Funct. Mater. 2024, 34, 2404495.

- [12] B. S. Parimalam, A. D. MacIntosh, R. Kadam, B. L. Lucht, J. Phys. Chem. C 2017, 121, 22733.
- [13] a) D. Qian, B. Xu, M. Chi, Y. S. Meng, Phys. Chem. Chem. Phys. 2014, 16, 14665; b) Z. Sun, Y. Zhao, M. He, L. Gu, C. Ma, K. Jin, D. Zhao, N. Luo, Q. Zhang, N. Wang, W. Duan, C.-W. Nan, ACS Appl. Mater. Interfaces 2016, 8, 11583.
- [14] C. D. L. Laffont, P. Gibot, M. Y. Wu, P. Kooyman, C. Masquelier, J. M. Tarascon, Chem. Mater. 2006, 18, 5520.
- [15] J. Wu, S. Weng, X. Zhang, W. Sun, W. Wu, Q. Wang, X. Yu, L. Chen, Z. Wang, X. Wang, Small 2023, 19, 2208239.
- [16] B. N. Olana, L. H. Adem, S. D. Lin, B.-J. Hwang, Y.-C. Hsieh, G. Brunklaus, M. Winter, ACS Appl. Energy. Mater. 2023, 6, 4800
- [17] a) S. Leroy, H. Martinez, R. Dedryvère, D. Lemordant, D. Gonbeau, Appl. Surf. Sci. 2007, 253, 4895; b) X. Teng, C. Zhan, Y. Bai, L. Ma, Q. Liu, C. Wu, F. Wu, Y. Yang, J. Lu, K. Amine, ACS Appl. Mater. Interfaces 2015, 7, 22751; c) M. Metzger, B. Strehle, S. Solchenbach, H. A. Gasteiger, J. Electrochem. Soc. 2016, 163, A798.
- [18] a) X. Liu, T. Zhang, X. Shi, Y. Ma, D. Song, H. Zhang, X. Liu, Y. Wang, L. Zhang, Adv. Sci. 2022, 9, 2104531; b) J.-G. Han, K. Kim, Y. Lee, N.-S. Choi, Adv. Mater. 2019, 31, 1804822.